

## *7. Future Near Detectors for Long Baseline Neutrino Oscillation Experiments*

in this study.

Further improvements to the fitting framework could also help achieve the full potential of an HPTPC. With the increase in statistics future experiments will benefit from, events could be binned in more than two variables. This would allow better characterisation of interactions, and so systematics could be applied to the target events more accurately. The systematics themselves could also be generated to be more appropriate for use with transverse kinematics. The systematics used in this study were designed to depend on the leptonic information in the event. As the lower detection thresholds allow better measurements of the hadronic side of interactions, models constructed to use this information would better use the full constraining power of an HPTPC.

However, this study does show that just by lowering detection thresholds and using different kinematic variables, systematic uncertainties gain an improvement in constraint, which will allow better distinguishing of models.

*Beef up conclusion.*

## 2. Neutrino Physics

Neutrinos are spin-1/2 fermions with extremely small mass and zero electric charge. They only interact via the weak and gravitational forces, allowing them to travel great distances through matter without ever being affected by it, and so making them very difficult to detect. This has made neutrinos one of the most elusive particles, despite being one of the most abundant in the Universe.

This chapter gives an overview of the history of neutrino physics, from Wolfgang Pauli's "desperate remedy" of an undetectable particle, to the 2015 Nobel prize winning results of SK [21] and SNO [22], as well as the relevant theory involved. Section 2.1 describes the initial evidence of the existence of neutrinos, and the discovery of the different flavours. The evidence of neutrino oscillations is presented in Section 2.2, separated by neutrino source. The theory behind the oscillation mechanism is introduced in Section 2.3, along with a discussion on the different interaction types relevant for long baseline neutrino oscillation experiments. Finally, Section 2.4 gives an overview of the current experimental status of neutrino oscillations, and the questions yet to be answered.

### 2.1. Neutrino Discovery

In 1933, using a magnetic spectrometer and a Geiger counter, Chadwick [23] measured a continuous energy spectrum of  $e^-$  from  $\beta$  decay. This appeared to violate the conservation laws for energy, momentum, and spin. This is because, assuming a two-body process, the emitted particle is carrying away the energy difference between the initial and final nuclear states, which should be constant, as is the case for  $\alpha$  and  $\gamma$  decays. However, the vast majority of the emitted  $\beta$  particles measured had energies much lower than the expected value, but none had energies higher.

Neils Bohr initially proposed a statistical formulation of the conservation laws, suggesting individual decays could violate them as long as the overall average resulted in no net change. However, the upper limit on the measured  $\beta$  energies, which was confirmed by Ellis and

## 2.2. Neutrino Oscillations Evidence

Neutrino oscillations are now well established, with many experiments measuring various aspects of the phenomena in different regimes. This was not always the case, however. In this section, the early evidence for oscillations of all flavours, and potential steriles, is discussed.

### 2.2.1. Solar Neutrinos

Electron neutrinos are produced in the Sun by a number of different mechanisms. The largest flux comes from the nuclear fusion of four Hydrogen atoms into a Helium (the *pp* chain):

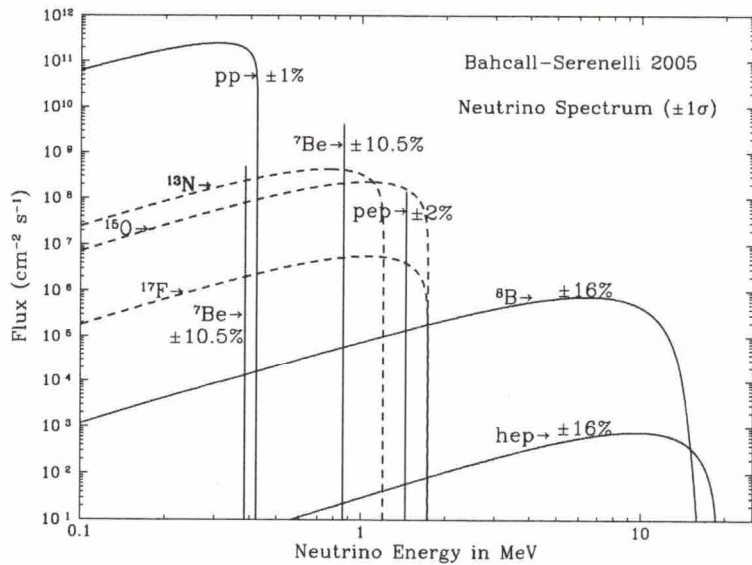


Figure 2.2.: Flux of solar neutrinos at Earth as a function of energy for different production mechanisms, according to Bahcall's solar model. Figure from [2].

However, the energy of the resulting neutrinos is below detection threshold. Other mechanisms produce higher energy neutrinos but with a lower flux, as shown in Figure 2.2. Most solar neutrino experiments therefore measure the flux produced through boron decay:



Ray Davis and John Bahcall devised an experiment to measure the flux of neutrinos pro-

## 2. Neutrino Physics

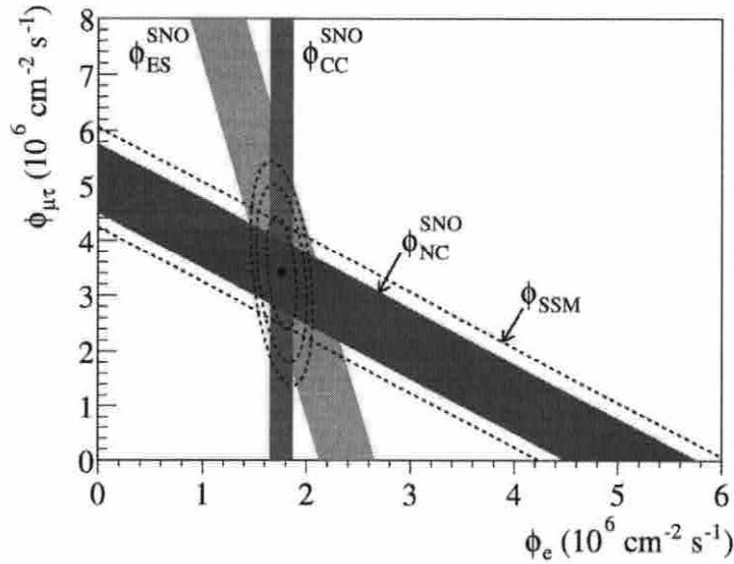


Figure 2.3.: The flux of  $\mu + \tau$  vs  $e$   ${}^8\text{B}$  solar neutrinos measured at SNO. The dashed lines show the total flux predicted by the BP2000 solar model [3]. The blue, red, and green bands show the flux measured through NC, CC, and elastic scattering reactions respectively. The intersect of the bands is at the bestfit values for  $\phi_e$  and  $\phi_{\mu\tau}$ , showing that the combined fluxes are consistent with the prediction. Figure from [4].

peaking between 1-10 GeV.

Reines [41] first measured the atmospheric neutrino flux at the Kolar Gold Fields mines in India in 1965. The measured flux was lower than had been predicted, a result which was confirmed by the IMB [42] and Kamiokande [43] experiments. The deficit was statistically convincing, but not significant enough to be considered compelling evidence of neutrino flavour change. These results became known as the Atmospheric Neutrino Anomaly.

The upgrade to the Kamiokande experiment, Super Kamiokande (SK), measured the flux of atmospheric  $\nu_\mu$  as a function of incoming angle in 1998. The data was split into upwards-going and downwards-going samples, allowing measurements at different distances from production. Upward-going neutrinos would have to travel through the Earth before reaching the detector, not just the distance from the atmosphere to the surface. In theory, since the neutrinos are produced isotropically in the atmosphere, there should be the same amount of upward-going and downward-going neutrinos. However, a large deficit of  $\nu_\mu$  was observed in the upward sample, as shown in Figure 2.4.

The dependence of the number of  $\nu_\mu$  observed on the distance travelled could be explained in the context of neutrino flavour mixing. The upward-going neutrinos were changing flavour

## 2.2. Neutrino Oscillations Evidence

as they propagated the longer distance through the Earth to the detector. The SK result was strong evidence of  $\nu_\mu$  disappearance through oscillation.

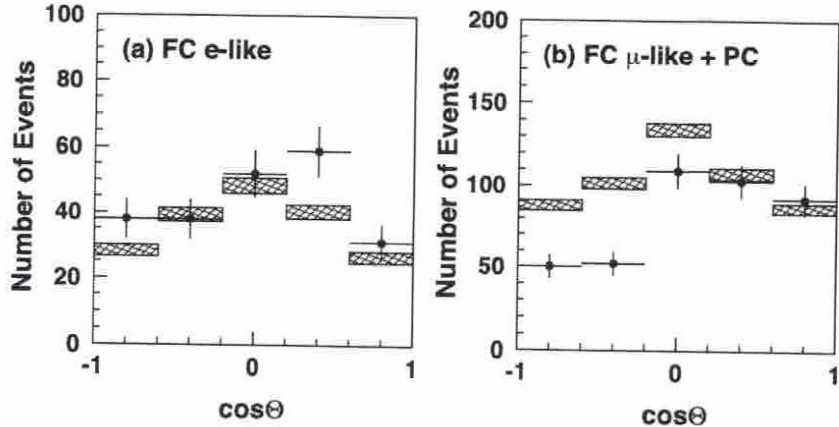


Figure 2.4.: The atmospheric neutrino flux as a function of angle from the first 414 days of Super-Kamiokande data. The boxes represent the prediction, the crosses represent the measured counts. Figure from [5].

### 2.2.3. Reactor Neutrinos

Reactor neutrinos have a similar energy flux to the solar neutrinos, peaking between 1-10 MeV. Like atmospheric neutrinos, experiments for detecting reactor neutrinos can measure oscillations across different baselines.

The KamLAND experiment [44] measured the  $\bar{\nu}_\mu$  flux from 55 nuclear power reactors across Japan, with a flux-weighted average baseline of 180 km. This gave sensitivity to  $\Delta m_{21}^2$ . The number of  $\bar{\nu}_\mu$  detected was smaller than would be expected if neutrinos could not change flavour, and the measured probability of oscillation as a function of energy and distance was in agreement with Pontercorvo's theory of neutrino flavour mixing. This provided further evidence that neutrinos oscillate while propagating through space.

There are several reactor experiments, RENO [45], Double Chooz [46], Daya Bay [47], with a shorter baseline of  $\sim 1$  km, sensitive to  $\theta_{13}$ . These have all measured an excess of neutrinos at  $E_\nu \sim 5$  MeV compared to prediction, which could be due to poor flux modelling, or the existence of sterile neutrinos.

### 2.2.4. Accelerator Neutrinos

More recently, accelerators have been used to produce beams of neutrinos to study oscillations. This offers more control over the energies and baselines involved. Most long baseline

### 2.3. Oscillation Theory

matrix, the sets of eigenstates would be identical and neutrinos would not change flavour, but the experimental evidence described in Section 2.2 shows this is not the case. The PMNS matrix is often expressed in the form:

$$U = \begin{pmatrix} U_{e1} & U_{e2} & U_{e3} \\ U_{\mu 1} & U_{\mu 2} & U_{\mu 3} \\ U_{\tau 1} & U_{\tau 2} & U_{\tau 3} \end{pmatrix} \quad (2.16)$$

Each element,  $U_{\alpha i}$ , corresponds to the amplitude of the mass eigenstate  $i$  within the flavour eigenstate  $\alpha$ . The flavour contents are shown in Figure 2.5, according to current best measurements. The left hand side is for the normal mass hierarchy, where  $m_3^2 > m_2^2$ , whereas the right hand side is for the inverted mass hierarchy, where  $m_2^2 > m_3^2$ . It is known that  $m_2^2 > m_1^2$  from solar neutrino measurements, but the nature of the mass hierarchy is not known beyond this. The signs of  $\Delta m_{32}^2$  and  $\Delta m_{31}^2$  are difficult to determine because the uncertainties on their values are so much larger than the size of  $\Delta m_{21}^2$ . The sign therefore is negligible in oscillation calculations in experiments, compared to the uncertainties.

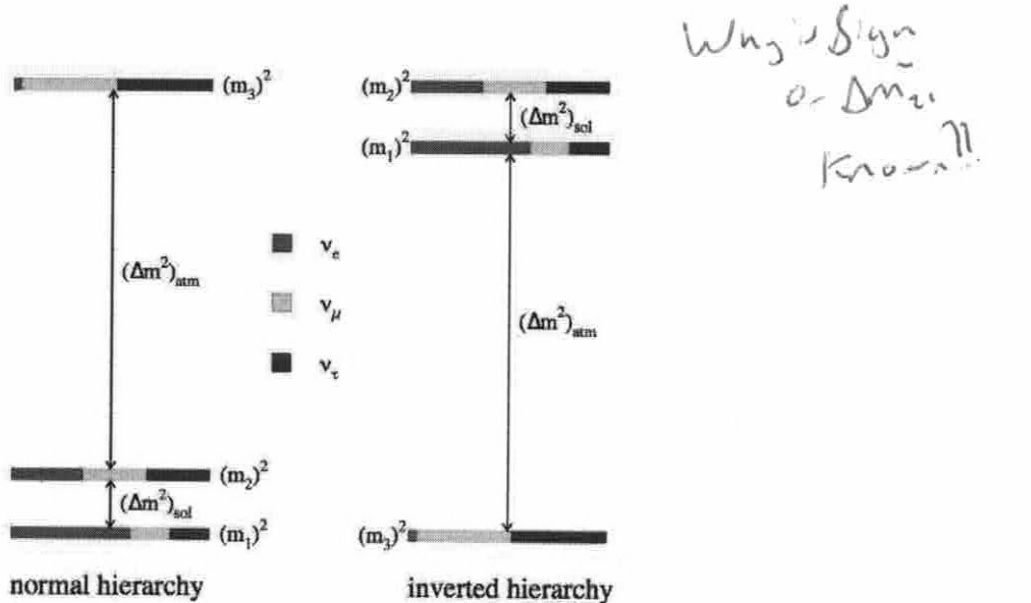


Figure 2.5.: The flavour content and mass differences of the three mass eigenstates, for both the normal and inverted hierarchies. Figure from [6].

The propagation of the mass eigenstates can be described by solutions to the plane wave equation:

$$|\nu_i(t)\rangle = e^{-i(E_i t - \vec{p}_i \cdot \vec{x}_i)} |\nu_i(0)\rangle, \quad (2.17)$$

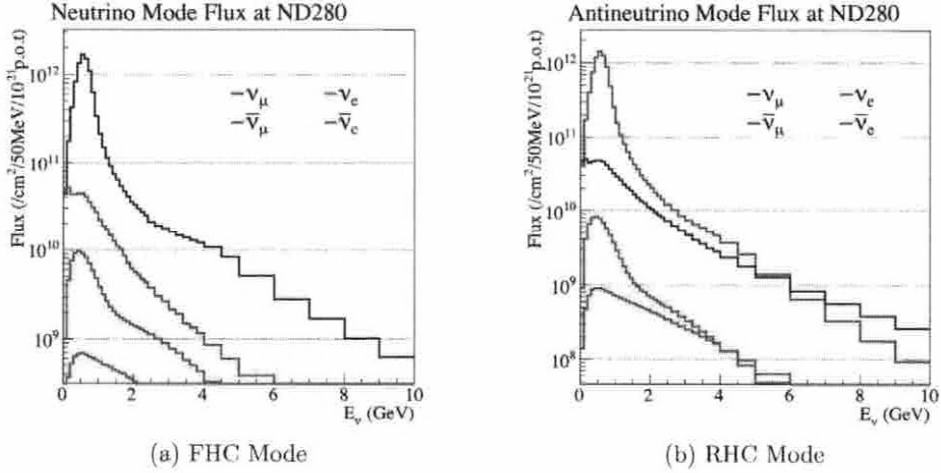


Figure 3.5.: Prediction of ND280 event rate broken down by neutrino species.

in FHC, and:

$$\begin{aligned} \mu^- &\rightarrow e^- + \bar{\nu}_e + \nu_\mu \\ K^- &\rightarrow \pi^0 + e^- + \bar{\nu}_e \end{aligned} \quad (3.4)$$

in RHC.

*N decay is also wrong sign. This is in the equations but not the text.*

In each mode, there is some contamination of the wrong sign neutrino due to imperfect horn focusing, as shown in Figure 3.5. As this is worse for RHC mode, and as anti-neutrinos have a much smaller cross-section than neutrinos, there are many more neutrino interactions in RHC mode than anti-neutrino interactions in FHC mode.

After the decay channel, there is a beam dump made up of 3.17 m of graphite and 2.4 m of iron. This stops all surviving mesons, and all muons below 5 GeV. Neutrinos and higher momentum muons reach the muon monitor (MUMON) beyond the beam dump. The MUMON consists of two independent detectors: Si PIN photodiodes, and ion chambers. These measure the muon profile on a bunch by bunch basis, which is a reliable measure of the beam direction and intensity as the majority of neutrinos in the beam are produced with a muon in a two-body decay. The MUMON measures the beam direction to an accuracy of 0.25 mrad, and the beam intensity to a precision of 3% [87].

It's not possible to count the total number of neutrinos produced in the beam, so the number of protons impinged on the target (POT) is used as a metric for the data collected by T2K. The total accumulated POT and beam power have been increasing since data

present in the event. Events with no other track can't have a reconstructed pion, so cannot be treated as CC  $1\pi$  or Other.

- **Bunch Matching:** The secondary track must be in the same time bunch as the muon candidate track. This cut rejects secondary tracks which are likely not from the same event.
- **Track Start Matching:** The secondary track must originate from the fiducial volume of the same FGD as the muon candidate track. Secondary tracks starting in a different detector are likely not from the same interaction so are rejected.
- **TPC Matching:** If the secondary and muon candidate tracks start in FGD1, the secondary track must also enter TPC 2. If the secondary and muon candidate tracks start in FGD2, the secondary track must also enter TPC 3. This cut ensures the secondary track is forward-going and long enough to be reconstructed.
- **TPC Quality:** There must be at least 18 clusters in the TPC. This cut ensures the track is large enough to be accurately reconstructed.
- **Pion PID:** The number of charged pions is determined by the number of secondary tracks with PID determined in the TPC corresponding to a pion. For positive tracks, the pion, positron and proton hypotheses are tested. For negative tracks, only the pion and electron hypotheses are tested. The pulls for each hypothesis are calculated and protons are rejected by requiring:

$$\frac{L_\mu + L_\pi}{1 - L_P} > 0.8, \quad (5.8)$$

for tracks with  $p < 500$  MeV/c. Muons are then rejected by requiring:

$$L_\pi > 0.3. \quad (5.9)$$

How well can  
the TPC separate  
 $\mu$  and  $\pi$   
↓  
general  
discussion.

The number of neutral pions is determined from the presence of positrons and electrons produced in their decay.

There are two methods by which information from an FGD can be used to identify if a particle with momentum too low or angle too high to enter a TPC is a pion. However, this can only be done for charged pions as electrons and positrons are not reconstructed.

### 5.3. Binning

including the original uniform rectangular binning which can still be used for validations of the changes to the fitting framework, and cross-group checks with the other near detector fitter which did not move to non-uniform rectangular binning.

The following algorithm was used to define a non-uniform but still rectangular binning for each sample, without having to have the same binning for FGD1 and FGD2:

- The bin edges on the  $\cos\theta$  axis are hard coded and constant, guided by the previous binning, keeping the bins rectangular. The reasons for this are discussed later in this section.
- For each  $\cos\theta$  row, scroll across from 30 GeV down 0 GeV in 100 MeV steps.
- Once 50 unscaled MC events are reached, start a new bin.
- If the last bin in a row (the lowest momentum bin) has <20 unscaled MC events, merge with the previous bin. Scroll through this merged bin in 5 MeV steps and split once half the events in the bin are reached.

The aim of this process was to produce as uniform a distribution of events across the bins as possible. This was not always possible, as regions of high density would require bins so small that they go below the resolution of the detector. The hard coded  $\cos\theta$  bin edges and momentum step sizes of 100 MeV were driven by this minimum bin size limit. The resolutions are calculated by plotting the reconstructed vs true kinematic variables, as shown in Figure 5.6, and taking the RMS at different slices of the 2D Gaussian. These RMSs, shown in Figures 5.7, give a gauge of the detector resolution, and so the minimum bin width for each variable in different regions.

For momentum, the RMS is fairly constant at approximately 100 MeV, for a momentum  $> 1000$  MeV. It then reduces linearly between 1000 and 400 MeV, before levelling off at approximately 60 MeV below 300 MeV. Similarly, for the angle, the RMS is constant at approximately 0.08 below 0.96. It then reduces linearly up to a  $\cos\theta$  of 1.0. However, given there would be a large uncertainty on the gradient for each variable's RMS, rather than varying the minimum bin size to trace out the change in RMS as closely as possible, it was safer to have a constant minimum size for all regions. This was chosen to be 0.01  $\cos\theta$  in angle, and 100 MeV in momentum to be sure they are above the resolution in all regions. Furthermore, as the  $\cos\theta$  systematics are better controlled than for  $p_\mu$ , and for aiding the simplicity of optimising the binning algorithm, the bins were kept constant in  $\cos\theta$ .

The distribution of events binned by the scheme produced using the algorithm are shown in Figure 5.8. Full templates of the binning for each sample are shown in Appendix A, as

Discuss  
M<sub>1</sub>/det, b<sub>1</sub> b<sub>2</sub> b<sub>3</sub> b<sub>4</sub> b<sub>5</sub>  
20 bins, scan p<sub>μ</sub> to 600.

### 6.1. Nominal MC

coherent events for FHC  $\nu$  and RHC  $\bar{\nu}$ .

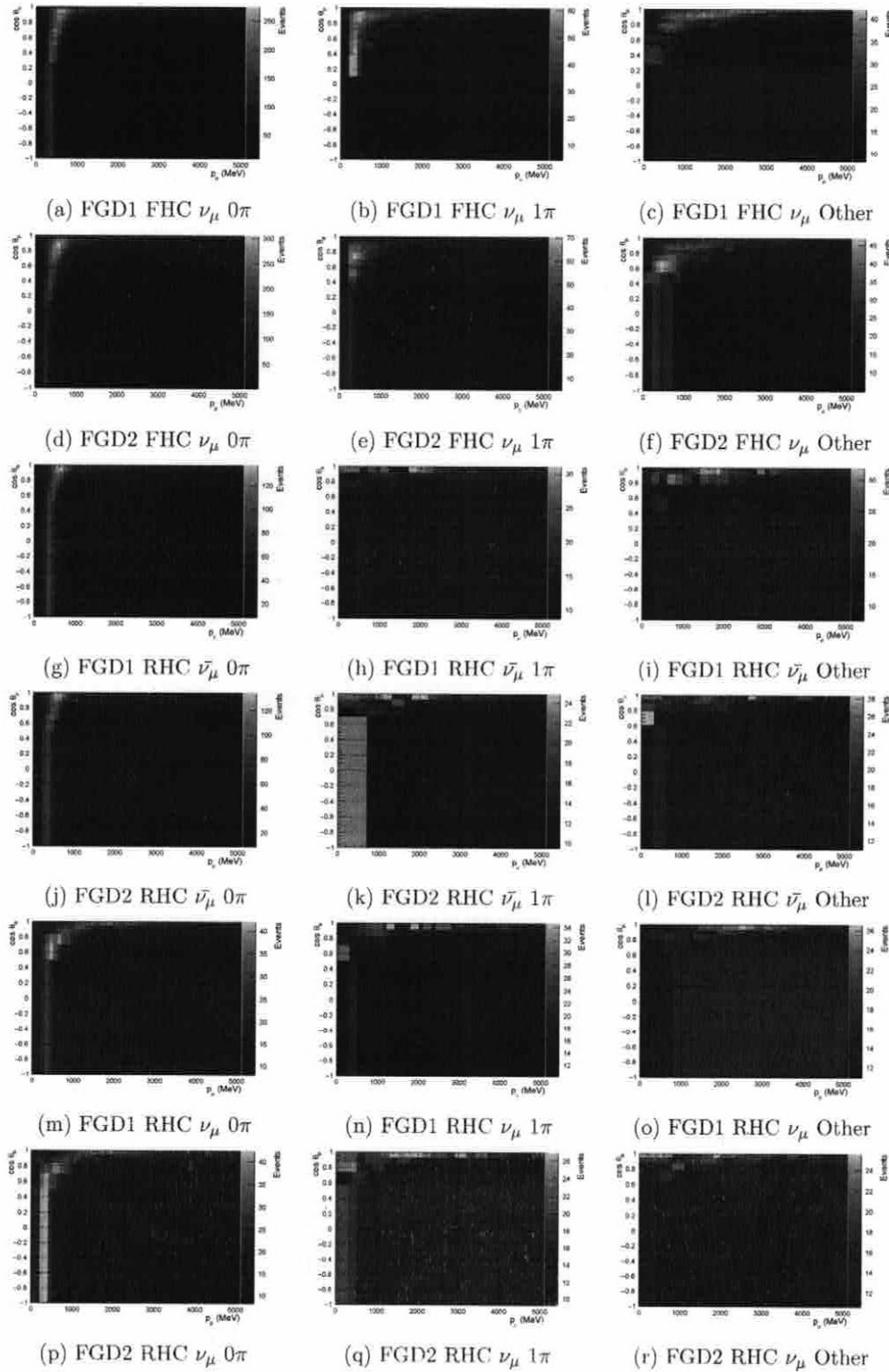


Figure 6.1.:  $p_\mu$ - $\cos \theta_\mu$  distributions for the nominal MC with non-uniform rectangular binning.

## 6.8. Oscillation Parameter Sensitivity

small amount higher. The differences in the RHC  $1R_\mu$  sample are very similar as for FHC  $1R_\mu$ , but the height and location of the peaks are identical in all three fits.

The predictions for the FHC  $1R_e$  sample has a higher peak for the uniform fit binning fit. Above and below the peak energy, the non-uniform fit binning predictions are slightly higher. This is a larger effect at lower energies.

For the RHC  $1R_e$  sample, the three predictions are very consistent. For the uniform fit binning, the event rate is slightly smaller at low energies than for the other fits, but the difference is very small.

The predictions for the  $1R_e$  1d.e. sample are also compatible across all energies. However, the peak is lower for the non-uniform fit and detector binning. This is the only region in any of the samples where the two non-uniform fit binning predictions aren't closer to each other than the uniform binning. Here, the non-uniform fit and merged-uniform detector binning event rate is slightly lower than the for the uniform binning, but this difference is smaller than the difference to the non-uniform fit and detector binning.

Overall, the three fit predictions are very compatible, with similar shapes and differences to the prior prediction. All the differences between the three posterior predictions are within the predicted uncertainties.

As the aim of the non-uniform binning was to improve the sensitivity, it is perhaps disappointing that the uncertainties on the event rates at SK are not smaller for the non-uniform binning fits. However, looking at just the event rate does not take into account the changes in shape and so does not tell the whole story. The full impact on the sensitivity to oscillation measurements is discussed in Section 6.8.2.

*-Can you point to specific improvements here?*

## 6.8. Oscillation Parameter Sensitivity

To see the full effect of all the updates to the near detector fit on the oscillation analysis, joint Asimov fits were run. These fit the ND280 and SK MC to the ND280 data and SK nominal MC.

Like for the SK posterior predictions, the oscillation parameters are set to the values in Table 6.6, and the SK detector parameters are set to their nominal values. The priors on  $\sin^2\theta_{23}$ ,  $\Delta m_{32}^2$ ,  $\delta_{CP}$ , and  $\sin^2\theta_{13}$  are flat for these fits. The solar parameters,  $\sin^2\theta_{12}$  and  $\Delta m_{12}^2$ , which T2K has little sensitivity to, have Gaussian priors from the PDG [14].

The ND280 fit binning used is the non-uniform binning defined in Appendix A. However, the detector binning is the 574 merged-uniform bins, as using the fit binning as detector

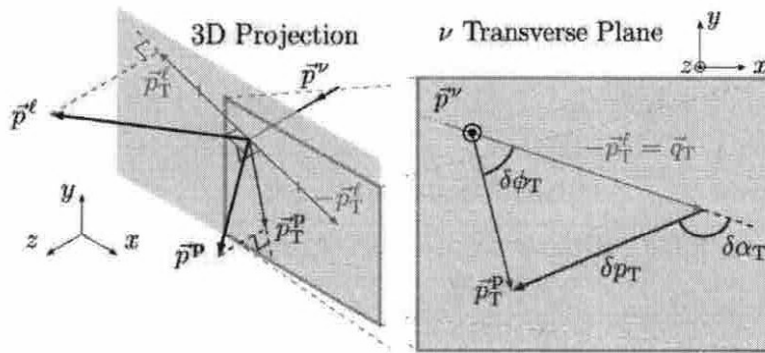


Figure 7.3.: Definition of the single transverse variables. Figure from [13].

Plane is  $\nu$ - $k$  plane. - Meisterkarte said.

These kinematics are also less dependent on the true incoming neutrino energy, which is not precisely known for individual events in accelerator neutrino experiments. Using these transverse variables can therefore provide insight into final state interactions and nuclear effects [134].

### 7.1.2. Sensitivity Studies

*✓ Simulation*  
HPTPC MC was produced to explore the potential sensitivity improvement from using an HPTPC. This was done by smearing the true kinematics of a subset of ND280 FGD1 MC events. For each event, for both the momentum and angle of the final state lepton, a random number was drawn from a Gaussian with mean equal to the value of the variable in the ND280 MC, and width equal to the assumed resolution of the HPTPC. The assumed resolutions are shown in Table 7.1.

- true.

The selection of events is similar to that described in Section 5.2, but using the full FGD1 volume. The assumed detection thresholds were different for the ND280 and HPTPC selections, as shown in Table 7.2. The thresholds are the only differences between the ND280 and HPTPC MC.

The selected events are then divided by pion and proton multiplicity, giving seven samples in total:

- **CC 0π 0p:** 1 muon above threshold, 0 charged pions above threshold, 0 protons above threshold.
- **CC 0π 1p:** 1 muon above threshold, 0 charged pions above threshold, 1 proton above threshold.